Spatial phase filtering approach for the instantaneous measurement of the degree and angle of linear polarization employing a pixelated polarization camera

D. I. Serrano-García, Y. B. Machuca-Bautista, J. L. Flores, G. A. Parra-Escamilla, and J. Cervantes-L.

University Center for Exact Sciences and Engineering, Guadalajara University, Blvd. Gral. Marcelino García Barragán 1421, 44430 Olímpica, Guadalajara, Jal. México.

H. O. González Ochoa

Departamento de Física, Universidad de Guadalajara, Blvd. Marcelino García Barragán 1421, 44430, Guadalajara, Jal. México.

B. Reyes-Ramírez

Instituto Nacional de Astrofísica Óptica y Electrónica, Luis Enrique Erro No. 1, Colonia Santa María Tonantzintla, 13700, Puebla 72840, México

Received 25 June 2024; accepted 9 March 2025

We present a novel phase-based filtering algorithm designed to retrieve the Degree of Linear Polarization (DoLP) and Angle of Linear Polarization (AoLP) by leveraging the intrinsic properties of a pixelated polarization camera. Unlike conventional intensity-based filters, our approach utilizes complex phase values to estimate polarization parameters, offering a flexible and computationally efficient alternative. Each point is treated as an independent measurement, dependent solely on the kernel size, which enables the potential for real-time processing. Experimental and simulation evaluations under Gaussian noise conditions validate the robustness of our approach, demonstrating a high degree of consistency with standard methods. The ANOVA analysis results reflect this consistency across datasets, as indicated by the sum of squares (SS), mean squares (MS), and F-statistic values. This reinforces the reliability of the proposed algorithm and highlights its practical applicability in noise-affected environments. Our findings suggest that the proposed method provides a stable and adaptable solution for polarization parameter extraction, making it well-suited for applications in fields such as biomedical imaging, remote sensing, and industrial inspection, where real-time performance and noise resilience are critical.

Keywords: Polarized light; mueller matrix; optical instrumentation.

DOI: https://doi.org/10.31349/RevMexFis.71.051302

1. Introduction

Polarization imaging cameras have been employed in various fields due to their unique characteristics, such as reducing reflection, contrast enhancement, scratch inspection, object detection, among others. These imaging sensors succeed by improving several conditions; for example, for increasing contrast characteristics of an image under test by detecting the angle of polarization of the reflected polarized light. Polarization-sensitive images also address the issue of unwanted reflections in acquired images coming from the environment. A typical implementation is stress inspection, where polarized light traveling through transparent media changes angle due to stressed areas, so the incoming angle of the polarized light will change to a different angle due to the areas of stress in the object. In profilometry, pixelated polarization cameras play an essential role when employed to retrieve optical devices' surface texture. In the object detection field, by employing polarized sensitive metrics helps distinguish objects [1,2]. While polarization imaging cameras have proven effective in specific applications, their performance is often limited by noise susceptibility, calibration challenges, and the rigidity of pixelated polarizer configurations. Existing solutions, including spatial and frequency domain filters and demosaicking techniques, fail to provide a comprehensive solution for dynamic environments, particularly outdoors. However, their effectiveness is often compromised by challenges such as noise susceptibility, calibration difficulties, and the inflexibility of pixelated polarizer configurations. The polarization imaging camera is composed of a micro-polarizer mask aligned with the imaging sensor; as a result of this arrangement, each pixel will carry a polarizer in its direction, making it possible to measure linear polarization parameters instantaneously. Some current challenges and limitations include Noise Susceptibility [3]. Polarization cameras are prone to various noise types, including additive noise and Poisson-shot noise, which can degrade image quality and the accuracy of polarization measurements. Effective denoising while preserving critical polarization information remains a significant challenge. Commonly, the micro-polarizer mask is composed of a pattern of polarizers with four orientations at $0°$, $45°$, $-45°$, and $90°$. This configuration is convenient for instantaneous measurements of the Degree of Linear Polarization (DoLP) and Angle of Linear Polarization (AoLP). Due to the specific architecture mentioned before, several authors have investigated diverse error models. The most common errors are the additive and the Poisson-shot noise [4-7]. Additionally, calibration of the

systems plays the primary role, where also you can find in the literature several calibrations [7,8] and filtering processes [8-10]. Accurate calibration is essential for reliable polarization measurements. Traditional calibration methods, such as single-pixel and super-pixel techniques, often fail to correct deviations in transmission, diattenuation, and orientation across the polarization filter array (PFA). These inadequacies can lead to errors in calculating the Angle of Linear Polarization (AoLP) and Degree of Linear Polarization (DoLP). For instance, filters at the frequency domain [11], spatial domain [12,13], and approaches using deep learning [14] are commonly found in the literature. Other authors have proposed demosaicking algorithms [15,16] and explored the enhancements through alternative polarized microgrid configurations [17]. Finally, the rigidity of pixelated polarizer configurations [18-20]. The fixed nature of micro-polarizer arrays limits adaptability to varying imaging conditions. This rigidity poses challenges in dynamic environments, particularly outdoors, where lighting and reflection conditions can change rapidly. We introduce a phase-based filter kernel that operates in the spatial domain, incorporating a flexible filter kernel designed to enhance instantaneous AoLP measurements. This method aims to improve noise resilience by leveraging phase information; the filter can more effectively distinguish between signal and noise, enhancing image quality. Enhance calibration accuracy; the adaptable nature of the filter kernel allows for better correction of transmission and orientation deviations across the PFA, leading to more precise polarization parameter calculations. Also, the method increases the flexibility of the proposed filter and adapts to varying imaging conditions, making it suitable for dynamic environments, including outdoor settings with changing illumination. The potential impact includes the implementation of the phase-based filter kernel, which could significantly advance polarization imaging by providing a more robust, accurate, and adaptable solution. This innovation can potentially enhance material property assessments, improve object detection accuracy, and expand the applicability of polarization imaging in diverse and dynamic environments. Here, we present a phase-based filter kernel that leverages the spatial domain and incorporates a flexibility filter kernel. Our algorithm offers improvements in instantaneous measurements of the AoLP parameter, which can be applied directly to various tasks, such as assessing material properties under diverse illumination conditions in sunlit outdoor environments [21].

2. Methods and material

2.1. Polarization measurements using a pixelated polarization camera

The polarization camera is equipped with a micro-polarizer array aligned with the imaging sensor; each pixel has a linear

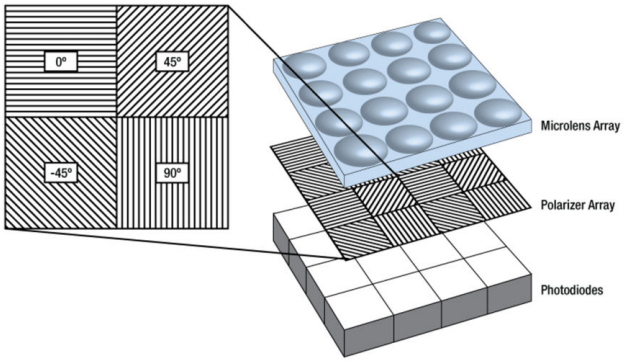

FIGURE 1. The four-directional wire grid polarizer array is located on the sensor chip, positioned between the microlens array and the photodiodes [22].

polarizer. We used a polarization camera KIRALUX model CS505MUP with a super-pixel with four orientations; as we show in Fig. 1. The wire grid polarizer array consists of a repeating pattern of polarizers oriented at 0°, 45°, $-45°$, and 90°, positioned on the sensor chip between the microlens array and the photodiodes. Each polarizer is composed of an array of parallel metallic wires, allowing the transmission of radiation with an electric field vector perpendicular to the wires while reflecting radiation with a parallel electric field vector. These pixel values are subsequently utilized to calculate three polarization parameters of the incident light at each pixel: intensity, degree of linear polarization, and azimuth. By embedding the polarizers in this location, crosstalk between adjacent polarizers is reduced, and alignment accuracy is enhanced compared to placing the polarizer array in front of the microlens array.

Using these pixel values, we can calculate the polarization parameters of the incident light at each pixel, including the degree of linear polarization, azimuth, and intensity. In our case, each super-pixel intensity can be represented as $I_1(i,j), I_2(i,j), I_3(i,j), I_4(i,j)$ corresponding to polarizer at the angle of 0°, 45°, $-45°$, and 90°, respectively. This arrangement allows each pixel (i,j) across the image can be demultiplexed according to its polarizer orientation

$$\begin{aligned} I_1(i,j) &= I(m,n), \\ I_2(i,j) &= I(m,n+1), \\ I_3(i,j) &= I(m+1,n), \\ I_4(i,j) &= I(m+1,n+1). \end{aligned} \tag{1}$$

Typically, by applying a linear combination of each intensity, two metrics can be determined instantly: the angle of Linear Polarization (AoLP) and the Degree of Linear Polarization (DoLP) [1,2] as

$$AoLP(i,j) = \tan^{-1}\left(\frac{I_4(i,j) - I_2(i,j)}{I_1(i,j) - I_3(i,j)}\right),$$

$$DoLP(i,j) = \frac{\sqrt{[I_4(i,j) - I_2(i,j)]^2 + [I_1(i,j) - I_3(i,j)]^2}}{I_1(i,j) + I_2(i,j) + I_3(i,j) + I_4(i,j)}. \quad (2)$$

With this approach, each intensity measurement is obtained from four pixels at different orientations, as previously mentioned.

2.2. Spatial phase filter

Our approach considers neighboring intensities to apply a filtering process requiring the initial determination of two parameters, the filtered total intensity term, namely $S_{0_f}(i,j)$ and the phase complex filtered term $\alpha(i,j)$ obtained as follows:

$$S_{0_f}(i,j) = \frac{1}{4}\sum_{k=i-a}^{i+a}\sum_{l=j-b}^{j+b}\big[I_1(k,l) \times +I_2(k,l) + I_3(k,l) + I_4(k,l)\big]h(k-i,l-j),$$

$$\alpha(i,j) = \prod_{k=i-a}^{i+a}\prod_{l=j-b}^{j+b}\left[\frac{I_1(k,l) - I_3(k,l)}{2} + \mathrm{i}\frac{I_4(k,l) - I_2(k,l)}{2}\right]^{h(k-i,l-j)}, \quad (3)$$

where $h(k,l)$ represents the (k,l) point of the convolution filter kernel, with horizontal and vertical sizes $2a+1$, and $2b+1$ respectively. Additionally, i denotes the imaginary unit and $I_1(k,l), I_2(k,l), I_3(k,l)$ and $I_4(k,l)$ the intensity at the pixelated polarization image. After calculating those two terms, the (i,j) measurement point of the filtered angle of linear polarization $AoLP_f(i,j)$ and filtered degree of linear polarization $DoLP_f(i,j)$ can be obtained as

$$AoLP_f(i,j) = \tan^{-1}\left[\frac{\alpha(i,j) - \alpha^*(i,j)}{\mathrm{i}(\alpha(i,j) + \alpha^*(i,j))}\right],$$

$$DoLP_f(i,j) = \frac{\sqrt{\alpha(i,j)\alpha^*(i,j)}}{S_{0_f}(i,j)}. \quad (4)$$

where * denotes the complex conjugate value, this approach allows us to obtain a filtered AoLP and DoLP parameters, considering neighbor pixels, employing a desired filter kernel h as can be average, Gaussian, among others. Figure 2 shows a schematic implementation of the algorithm, in the first step, the raw intensity values are captured from the sensor. Then, in step two, these intensities are arranged based on their respective polarization angles (0, 45, 90, and -45 degrees). Step three involves computing the total intensity term and the phase complex filtered term, which provide essential information about the light's characteristics. Finally, in step four, the Degree of Linear Polarization (DoLP) and Angle of Linear Polarization (AoLP) are derived, providing critical insights into the polarization characteristics of the scene.

Our filter process differs significantly from the other known methods. For instance, in Ref. [1], the authors introduced a convolution process based on intensity values for interferometric phase measurements. Furthermore, in Ref. [1], the author presents an error analysis of pixelated carrier algorithms and proposes a nine-point filter. In contrast, our algorithm operates based on the complex phase value, providing a general formula that can be used with different filtering kernel types and mask sizes.

3. Results

3.1. Numerical simulations

To test the feasibility of our proposal, we made two spatial distributions varying AoLP within the range of $[-\pi,\pi]$ and DoLP within the range of [0,1]. These distributions are presented in Figs. 3a) and 3b), respectively. Using these two parameters, we first modeled the pixelated intensity and added

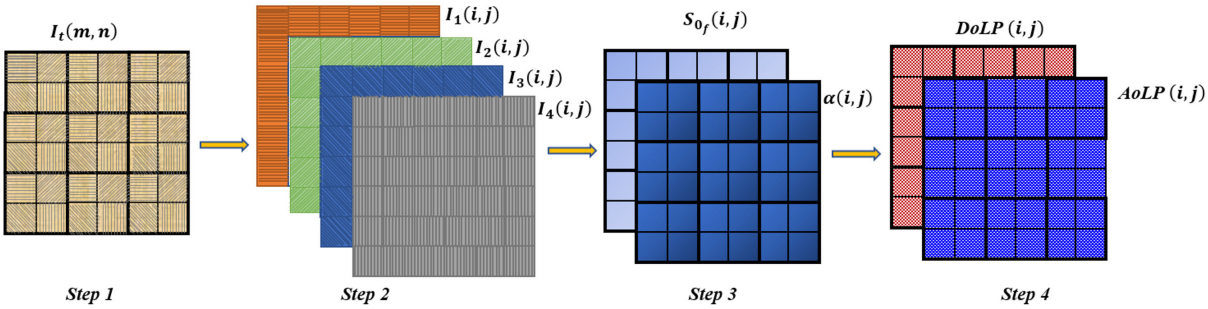

FIGURE 2. Diagram of the process for calculating the polarization parameters of incident light using a pixelated polarization camera. The procedure consists of four steps: (Step 1) acquisition of intensities in a super-pixel with different polarization orientations, (Step 2) organization of the measured intensities, (Step 3) calculation of the total intensity term, namely, $S_{0_f}(i,j)$, and the phase complex filtered term $\alpha(i,j)$, and (Step 4), the extraction of the filtered DoLP and AoLP metrics.

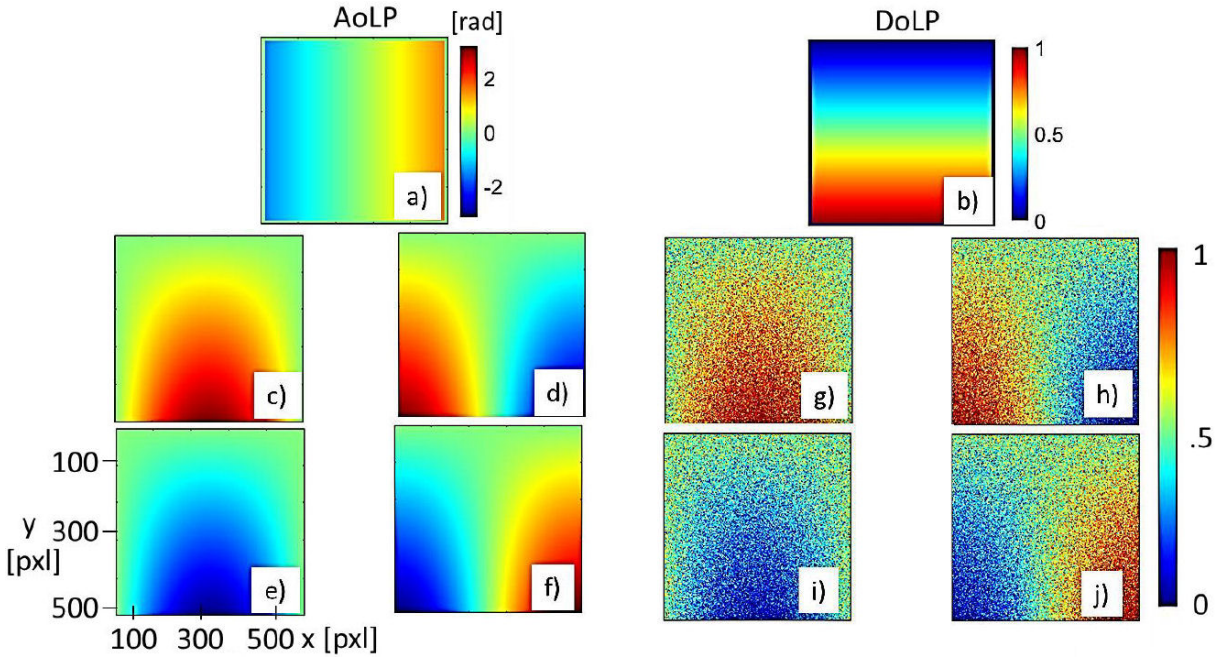

FIGURE 3. Shows the simulated AoLP a) and DoLP b) images used to test our filtering process. Figures c) to f) display the four intensities images without noise, while figures g) to j) show the intensity with added zero-mean Gaussian noise to emulate additive noise.

a simulated noise. For example, Figs. 3g) to 3j) illustrate the effect of additive zero-mean Gaussian noise and variance of 0.025 [3-6]. Figures 3c) to 3f) show the four demultiplexed intensities without noise, while Figs. 3g) to 3j) display the intensities with the simulated noise.

We analyzed our proposal against the intensity-based filter using a zero-mean Gaussian noise to emulate additive noise. Our simulations introduce an incremental error variance in each pixelated intensity, and as a metric, we considered the AoLP and DoLP root mean square (RMS) error. Figure 4a) and 4b) correspond to the case for the AoLP and DoLP respectively. The plots in Fig. 4 illustrate the filtering result using a Gaussian mask of 3×3 and standard deviation of 0.5. The solid line represents the standard intensity convolution filter and the $^\circ$ line shows our proposal method. As a result, our simulations show that our approach can be treated as an alternative to the intensity-based algorithm.

In order to crosscheck our proposal we made an ANOVA analysis. It aims to compare the proposed algorithm for calculating DoLP and AoLP with the standard approach. Separate ANOVA analyses were performed to assess whether the differences observed in AoLP and DoLP values between both methods are statistically significant. The results obtained are presented below, where SS is the sum of squares (SS) measures the variability in the data. It is calculated by summing the squared differences between observations and their mean, df is the degrees of freedom indicate the number of independent values available to estimate a statistical parameter, MS is the Mean square is the average variance, calculated by dividing SS by df, and finally F stands for the F-statistic in ANOVA is calculated as the ratio between $\mathrm{MS}_{(\mathrm{Groups})}$ and $\mathrm{MS}_{(\mathrm{Error})}$. A high F-value indicates that the variability explained by the groups is much larger than the unexplained variability, suggesting a significant effect. Table I and Table II show the results for AoLP and DoLP respectively.

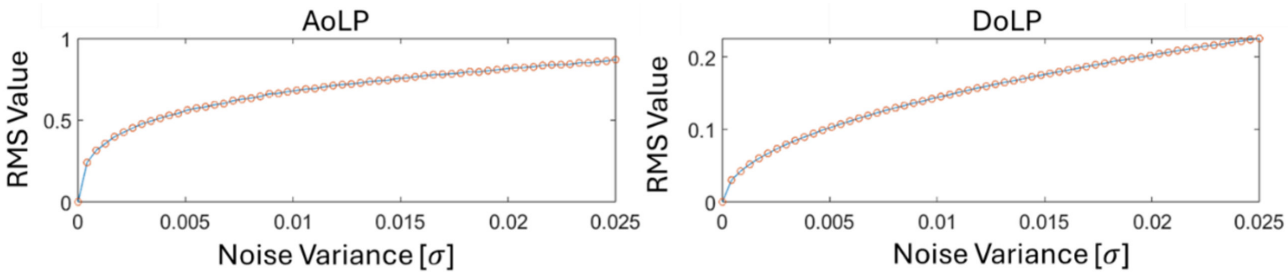

FIGURE 4. Root mean square error (RMSE) results for the AoLP and the DoLP metrics under additive noise. The solid line represents the response from the intensity filter, while the $^\circ$ line represents our proposed approach.

TABLE I. Results for Set1 of AoLP for Standard Method (SM) and our proposal (OP).

Source	SS		df		MS		F		Prob > F	
	SM	OP	SM	OP	SM	OP	SM	OP	SM	OP
Groups	35.552	35.552	59	59	0.6026	0.6026	1.27e+5	1.27e+5	0	0
Error	0.0054	0.0054	1140	1140	4.73e-6	4.73e-6	-	-	-	-
Total	35.5580	35.5580	1199	1199	-	-	-	-	-	-
p-value	0.0000	0.0000	-	-	-	-	-	-	-	-

TABLE II. Results for Set2 of DoLP for Standard Method (SM) and our proposal (OP).

Source	SS		df		MS		F		Prob > F	
	SM	OP	SM	OP	SM	OP	SM	OP	SM	OP
Groups	3.6173	3.6173	59	59	0.0613	0.0613	1.0368e+6	1.0368e+6	0	0
Error	6.74e-5	6.74e-5	1140	1140	5.913e-8	5.913e-8	-	-	-	-
Total	3.6174	3.6174	1199	1199	-	-	-	-	-	-
p-value	0.0000	0.0000	-	-	-	-	-	-	-	-

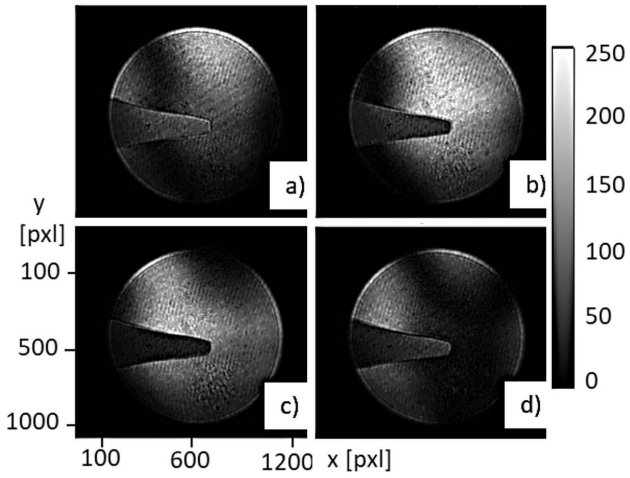

FIGURE 5. Experimental results obtained using a polarization Michelson type interferometer coupled to a pixelated polarization camera. Figures a) to d) show the four demultiplexed intensities.

The ANOVA analysis results for AoLP and DoLP indicate no significant differences between the two evaluated methods. This is evident from the identical values of SS, MS, and F in both datasets (Set 1 and Set 2). Although the p-value is extremely small ($p = 0$), suggesting statistically significant differences between the groups, the identical results across both datasets confirm that the proposed algorithm is consistent and produces results comparable to the standard method.

3.2. Experimental results

We tested our filtering algorithm using a polarization Michelson interferometer equipped with a KIRALUX CS505MUP polarization camera. This camera features a CMOS sensor and an on-chip wire grid polarizer array with a pixel size of 3.45×3.45 μm and a resolution of 5-megapixel. Detailed information about the interferometric system can be found in Refs. [24,25]. Figure 5a) to 5d) shows the four demultiplexed intensities corresponding to phase variation induced by a tin soldering iron placed on one arm of the interferometer.

Figure 6 presents the corresponding AoLP and DoLP information. Figures 6a) and 6b) display the AoLP and DoLP information without filter and Figs. 6c) and 6d) show the results after applying our filtering Gaussian mask of 7×7 pixels and a standard deviation of $\sigma = 1.5$. Figure 7 illustrates the traces marked in Fig. 6, where the upper plots compare the AoLP traces, showing the unfiltered data (blue line) and the filtered data with our method (red line). Similarly, the lower plots depict the DoLP traces under the same conditions.

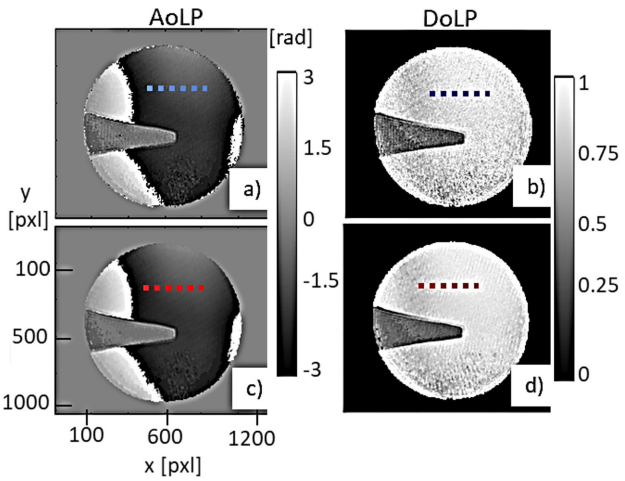

FIGURE 6. AoLP and DoLP images, where a) and b) correspond to the unfiltered images, while c) and d) show filtered images obtained using a 7×7 pixel Gaussian kernel with a standard deviation of $\sigma = 1.5$.

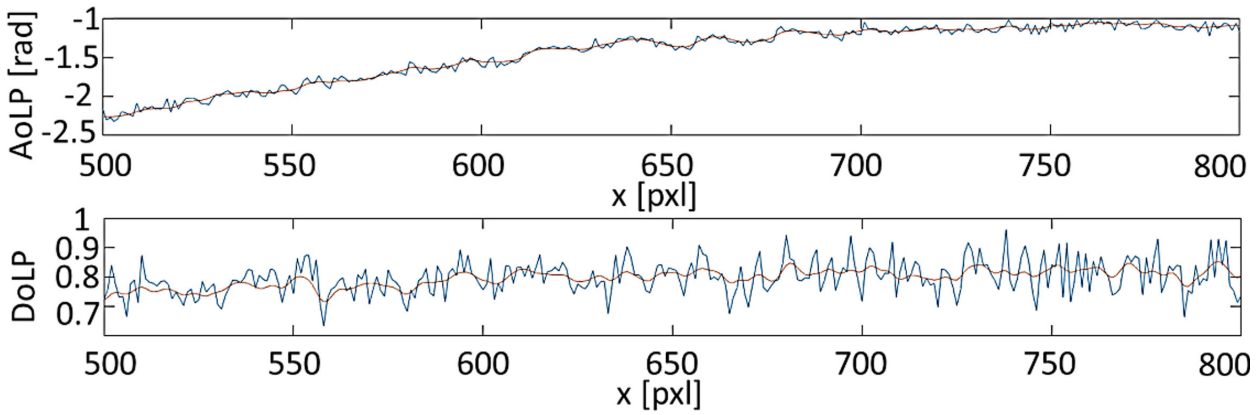

FIGURE 7. Plots marked at Fig 4 of the AoLP and DoLP information. The upper plot compares the AoLP trace for the unfiltered data (blue line) and the filtered data obtained with our proposal (red line). Similarly, the lower plot illustrates the DoLP trace under the same conditions.

4. Conclusions and final remarks

This study introduced a novel phase-based filtering algorithm aimed at enhancing the precision of Angle of Linear Polarization (AoLP) and Degree of Linear Polarization (DoLP) measurements in polarization imaging. Through extensive numerical simulations and experimental validations, we demonstrated that the proposed algorithm achieves performance comparable to conventional intensity-based convolution filters in terms of polarization parameter estimation. The results of the ANOVA analysis indicated no statistically significant differences between the proposed and standard methods, as reflected in identical values for the sum of squares (SS), mean squares (MS), and F-statistics across datasets. This suggests that the proposed algorithm provides consistent and reliable results on par with existing approaches. Despite the lack of statistically significant differences, the phase-based filtering approach offers advantages in terms of flexibility and robustness to challenging imaging conditions. Its adaptability to spatial variations and inherent noise resistance position it as a viable alternative for applications such as material characterization, biomedical imaging, and remote sensing, where stability and precision are critical factors. By achieving comparable performance to established methods, this work contributes to the ongoing development of polarization imaging technologies by providing a practical, adaptable, and computationally efficient alternative for polarization parameter extraction. The findings reinforce the potential of phase-based approaches in applications where real-time performance and resilience to noise are essential. Future work will focus on further refining the algorithm to enhance its computational efficiency and exploring its integration into advanced optical systems for applications in autonomous navigation, industrial quality control, and environmental monitoring.

Disclosures

The authors declare no conflicts of interest.

Data availability

Data underlying the results presented in this paper are not publicly available at this time but may be obtained from the authors upon reasonable request.

1. N. Brock, B. T. Kimbrough, and J. E. Millerd, A. pixelated micropolarizer-based camera for instantaneous interferometric measurements, *In Polarization Science and Remote Sensing V*, **8160** (2011) 81600W, https://doi.org/10.1117/12.892129
2. P. Yan *et al.*, Pixelated carrier phase-shifting shearography using spatiotemporal low-pass filtering algorithm, *Sensors* **19** (2019) 5185, https://doi.org/10.3390/s19235185
3. H. Liu *et al.*, Review of polarimetric image denoising, *Advanced Imaging* **1** (2024) 022001, https://doi.org/10.1088/2633-4356/abc123
4. S. Roussel, M. Boffety, and F. Goudail, Polarimetric precision of micropolarizer grid-based camera in the presence of additive and Poisson shot noise, *Optics Express* **26** (2018) 29968, https://doi.org/10.1364/OE.26.029968
5. J. Yang *et al.*, Temporal and spatial error model for estimating the measurement precision of the division of focal plane polarimeters, *Optics Express* **29** (2021) 20808, https://doi.org/10.1364/OE.429237
6. F. Goudail and A. BéniÃ¨re, Estimation precision of the degree of linear polarization and of the angle of polarization in the presence of different sources of noise, *Applied Optics* **49** (2010) 683, https://doi.org/10.1364/AO.49.000683
7. N. Hagen and Y. Otani, Stokes polarimeter performance: general noise model and analysis, *Applied Optics* **57** (2018) 4283, https://doi.org/10.1364/AO.57.004283

8. A. Giménez *et al*., Calibration algorithms for polarization filter array camera: survey and analysis, *Journal of Electronic Imaging* **29** (2020) 041011, https://doi.org/10.1117/1.JEI.29.4.041011
9. E. P. Wibowo *et al.*, An improved calibration technique for polarization images, *IEEE Access* **7** (2019) 28651, https://doi.org/10.1109/ACCESS.2019.2901892
10. Y. Giménez *et al*., Calibration for polarization filter array cameras: recent advances, *In Fourteenth International Conference on Quality Control by Artificial Vision*, **11172** (2019) 297, https://doi.org/10.1117/12.2523234
11. J. S. Tyo, C. F. LaCasse, and B. M. Ratliff, Total elimination of sampling errors in polarization imagery obtained with integrated microgrid polarimeters, *Optics Letters* **34** (2009) 3187, https://doi.org/10.1364/OL.34.003187
12. A. Abubakar *et al*., Performance Evaluation of Gaussian Noise Denoising Algorithms for DoFP Polarization Image Sensors, *In 2019 International Conference on Electrical and Computing Technologies and Applications* (ICECTA) (2019) 1, https://doi.org/10.1109/ICECTA48151.2019.8959603
13. B. T. Kimbrough, Pixelated mask spatial carrier phase shifting interferometry algorithms and associated errors, *Applied Optics* **45** (2006) 4554, https://doi.org/10.1364/AO.45.004554
14. X. Li *et al*., Learning-based denoising for polarimetric images, *Optics Express* **28** (2020) 16309, https://doi.org/10.1364/OE.393437
15. N. Li *et al.*, Demosaicking DoFP images using Newton's polynomial interpolation and polarization difference model, *Optics Express* **27** (2019) 1376, https://doi.org/10.1364/OE.27.001376
16. S. Liu *et al*., A New Polarization Image Demosaicking Algorithm by Exploiting Inter-Channel Correlations with Guided Filtering, *IEEE Transactions on Image Processing* **29** (2020) 7076, https://doi.org/10.1109/TIP.2020.2993109
17. B. M. Ratliff and G. C. Sargent, Alternative linear microgrid polarimeters: design, analysis, and demosaicing considerations, *Applied Optics* **60** (2021) 5805, https://doi.org/10.1364/AO.427752
18. N. Hagen and Y. Otani, Using polarization cameras for snapshot imaging of phase, depth, and spectrum, *Optical Review* **31** (2024) 359, https://doi.org/10.1007/s10043-024-00898-0
19. X. Pu *et al.*, Polarizing Camera Array System Equipment and Calibration Method, IEEE Transactions on Instrumentation and Measurement (2023), https://doi.org/10.1109/TIM.2023.3247389
20. C. Lane, D. Rode, and T. RÃ¶sgen, Calibration of a polarization image sensor and investigation of influencing factors, *Applied Optics* **61** (2022) C37, https://doi.org/10.1364/AO.447890
21. M. K. Kupinski *et al*., Angle of linear polarization images of outdoor scenes, *Optical Engineering* **58** (2019) 082419, https://doi.org/10.1117/1.OE.58.8.082419
22. Thorlabs, Polarization Camera with 5.0 MP Monochrome CMOS Sensor (n.d.), https://www.thorlabs.com/newgrouppage9.cfm?objectgroup_id=13033
23. B. T. Kimbrough, Pixelated mask spatial carrier phase shifting interferometry algorithms and associated errors, *Appl. Opt.* **45** (2006) 4554, https://doi.org/10.1364/AO.45.004554
24. G. A. Parra-Escamilla *et al*., Pixelated polarizing system for dynamic interferometry events employing a temporal phase unwrapping approach, *Optics Communications* **458** (2020) 124862, https://doi.org/10.1016/j.optcom.2019.124862
25. D. I. Serrano-García and Y. Otani, Dynamic phase measurements based on a polarization Michelson interferometer employing a pixelated polarization camera, *Advances in Optical Technologies* **6** (2017) 47, https://doi.org/10.1515/aot-2016-0050